https://doi.org/10.5194/egusphere-2026-5140
Preprint. Discussion started: 23 September 2026

Brief communication: First NISAR interferometric snow water equivalent change retrieval evaluated against airborne lidar

Zachary Hoppinen[1], Hans-Peter Marshall[2], Ross Palomaki[3], Coleman Kane[2], Siobhan Ciafone[4], Shad O'Neel[4], and Thomas Van Der Weide[2]

[1]Geophysical Institute, University of Alaska Fairbanks, 2156 Koyukuk Drive, Fairbanks, AK, USA
[2]Department of Geosciences, Boise State University, 1910 University Drive, Boise, ID 83725, USA
[3]Institute of Arctic and Alpine Research, University of Colorado, 4001 Discovery Dr, Boulder, CO 80303, USA
[4]Cold Regions Research and Engineering Laboratory, US Army Engineer Research and Development Center, 72 Lyme Road, Hanover, NH 03755, USA

Correspondence: Zachary Hoppinen (zmhoppinen@alaska.edu)

Abstract. NISAR's global L-band repeat-pass interferometry should be sensitive to snow water equivalent change (ΔSWE). We compare ΔSWE from an operational NISAR interferogram to near-coincident airborne lidar snow-depth change over a February 2026 pair in southwest Idaho. Across the scene, ΔSWE correlates well with the lidar depth change ($r = 0.82$, rising to $r = 0.93$ above a coherence of 0.2). The agreement is dominated by variability at scales above $\sim$1 km ($r \approx 0.94$), while the correlation at sub-kilometer scales is weaker ($r \approx 0.42$), improving over open terrain and at incidence angles below 50°. These results provide the first direct evidence that NISAR phase can measure dry-snow accumulation.

1 Introduction

Seasonal snow is a critical water resource, but no current method measures its water content, the snow water equivalent (SWE), across the scales and at the resolutions water management requires in mountainous terrain: at the tens to hundreds of meters over which SWE varies and over an extent that allows basin aggregates used in runoff forecasting (Dozier et al., 2016). Point sensors measure SWE accurately but sample single locations. Airborne lidar maps snow depth, not SWE, and only when and where it is flown. Numerical models struggle in complex terrain. Passive microwave retrievals saturate in deep snow and are too coarse for application in the mountains. Optical sensors map snow extent but not SWE.

Repeat-pass interferometric synthetic aperture radar (InSAR) can map changes in SWE (ΔSWE). The retrieval concept uses the fact that radar waves travel slower through snow than through air. New dry snow between two acquisitions therefore adds a travel time delay and a corresponding phase change that grows with ΔSWE (Guneriussen et al., 2001; Leinss et al., 2015). Airborne (Nagler et al., 2022) and satellite (Belinska et al., 2022; Ruiz et al., 2024) retrievals have demonstrated this. L-band SAR is well suited for this application: it penetrates dry snow with little signal loss, decorrelates slowly between passes, and passes through forest canopy better than shorter wavelengths (Bonnell et al., 2024).

The NASA-ISRO SAR mission (NISAR; Rosen et al., 2015) provides global L-band InSAR coverage at a regular 12-day repeat cycle, but whether its phase change can be used to estimate SWE change on the ground has not been tested. We provide

https://doi.org/10.5194/egusphere-2026-5140
Preprint. Discussion started: 23 September 2026

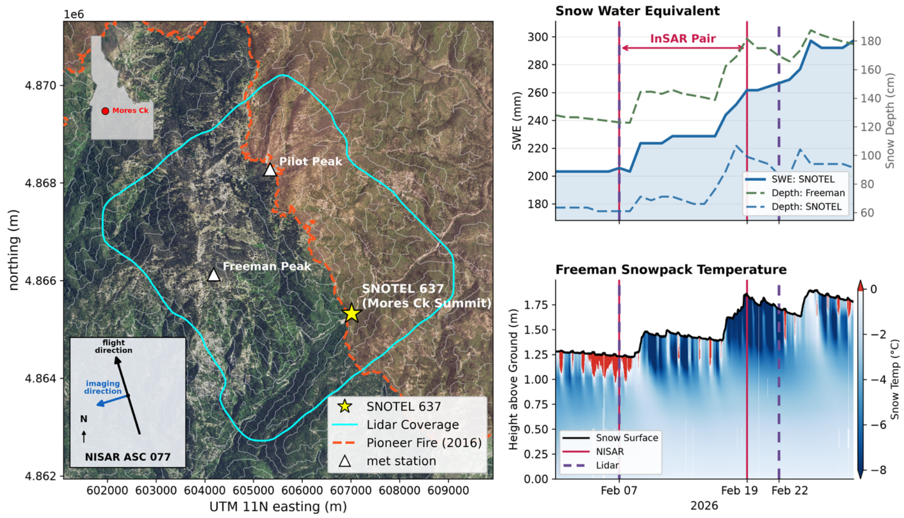

Figure 1. Study area and snow conditions at Mores Creek Summit, Idaho. Left: NAIP optical basemap with the NIVAL airborne-lidar coverage, in situ stations, the 2016 Pioneer Fire outline (to the east of the orange dashed line), the NISAR flight and look directions, and an Idaho locator inset. SWE at the Snow Telemetry (SNOTEL) station and snow depth at the SNOTEL and Freeman sites (right top) and the Freeman snowpack-temperature profile from the two acquisition dates (right bottom). Red marks snow within $0.1\,^{\circ}\mathrm{C}$ of melting. Our wetness criterion reads from $5\,\mathrm{cm}$ to $0.5\,\mathrm{m}$ below the surface, so a melting skin above it does not make an acquisition wet.

an initial test by comparing the spatial patterns of NISAR ΔSWE against snow-depth change (ΔH_s) from near-coincident NIVAL airborne-lidar surveys (Van Der Weide et al., 2026) over a NISAR pair at Mores Creek Summit, Idaho, USA.

2 Study area and conditions

Mores Creek Summit sits in the Boise National Forest, in complex terrain that includes forest, open ground, and a 2016 burn scar (Fig. 1). The NIVAL lidar flights were timed to coincide with NISAR ascending track 077, so we drew our candidates from the operational interferograms on that track. Seven of them have a lidar flight within a few days of each acquisition. Liquid water breaks the dry-snow phase relation assumed in Eq. (1) and decorrelates the pair, so both acquisitions must fall on a dry snowpack. We evaluate for dry snow using two instrumented sites within the scene. Six of the seven are wet at one or both acquisitions (Supplement), as water year (WY) 2026 was historically warm with many SNOTEL sites recording the lowest peak SWE in 85 years. The remaining pair, track 077 frame 024 imaged at the dawn overpass (05:46 local time) on February 7 and 19, 2026, is the one analyzed here. NIVAL airborne-lidar surveys of snow depth on February 7 and 22 (Van Der Weide et al., 2026) provide the validation.

The snowpack was cold and dry with significant accumulation across the pair (Fig. 1). At the first acquisition, the snow surface at the Freeman monitoring site ($\sim 2390\,\mathrm{m}$) was within a few tenths of $0\,^{\circ}\mathrm{C}$ while the pack averaged $-2.2\,^{\circ}\mathrm{C}$ through its depth. During the second acquisition, it was below freezing throughout, averaging $-5.7\,^{\circ}\mathrm{C}$ and ranging from $-19\,^{\circ}\mathrm{C}$ near the

https://doi.org/10.5194/egusphere-2026-5140
Preprint. Discussion started: 23 September 2026

surface to $-0.6\,^{\circ}\mathrm{C}$ at the base. Between the two, SWE rose by $56\,\mathrm{mm}$ and snow depth by $38\,\mathrm{cm}$ at the Mores Creek Summit SNOTEL (SNTL:ID:637, $\sim$1878 m), and by $58\,\mathrm{cm}$ at the nearby Freeman station. The accumulation was modest relative to NISAR's $\sim$24 cm wavelength and stayed within about one fringe (2π; Sect. 4). The Freeman station averaged $0.8\,\mathrm{m\,s^{-1}}$ wind speeds between acquisitions, with a peak gust of $4.1\,\mathrm{m\,s^{-1}}$, below the $\sim$$7\,\mathrm{m\,s^{-1}}$ threshold for the transport of fresh snow (Li and Pomeroy, 1997). The high alpine summit Pilot Peak station ($\sim$2470 m) gusted to $17\,\mathrm{m\,s^{-1}}$ but sustained winds were generally less than $7\,\mathrm{m\,s^{-1}}$. This suggests minimal redistribution of the new snow except at isolated exposed ridgelines (Hoppinen et al., 2026).

3 Data and methods

We use the operational NISAR L2 geocoded unwrapped interferogram for this pair, distributed by the Alaska Satellite Facility and produced with the ISCE3 software (Fattahi et al., 2023). The product is formed with 5 range by 6 azimuth looks (20 m resolution), unwrapped at 13 by 16 looks (80 m resolution), and is processing version P05023. The wrapped interferogram is therefore delivered at 20 m but the unwrapped phase only at 80 m. We work on both grids: the delivered 80 m phase carries the scene-wide comparison, and we unwrap the 20 m layer ourselves to resolve finer detail.

Atmospheric variations between acquisitions can introduce non-snow phase signals. The product comes with hydrostatic and wet tropospheric screens and a split-spectrum ionospheric screen as separate layers. We evaluated both: the tropospheric delay from the RAiDER screen (Maurer et al., 2021) carried in the product, and the ionospheric change from global maps of total electron content (TEC; Hernandez-Pajares et al., 2009) at the two acquisition dates. Both effects were minimal, so we applied neither atmospheric correction to the phase (Sect. 5).

We convert the unwrapped phase change ($\Delta\phi$) to ΔSWE using the dry-snow approximation of Leinss et al. (2015), building on Guneriussen et al. (2001), which does not require a density estimate:

$$\Delta\mathrm{SWE} = \frac{\lambda\,\Delta\phi}{2\pi\,(1.59+\theta^{2.5})} \tag{1}$$

where λ is the radar wavelength ($0.238\,\mathrm{m}$ at L-band) and θ is the local incidence angle in radians, derived from the NISAR line-of-sight vectors and the Copernicus GLO-30 digital elevation model (DEM) (European Space Agency and Airbus, 2021). Interferometric phase is relative and needs to be fixed to a reference point. We anchor it with a single constant offset (not tied to a field measurement) that removes the median bias between ΔSWE and the lidar-implied SWE ($\Delta\mathrm{H_s}$ converted using the SNOTEL-derived new snow density of $147\,\mathrm{kg\,m^{-3}}$). Because it is a scene-wide constant, this leaves the spatial pattern and the correlation unchanged. Our comparison, therefore, tests the spatial pattern of ΔSWE, not its absolute level, so this choice of reference point does not affect the comparison presented here.

We compare the retrieval to depth change from the two NIVAL lidar snow-depth surveys, $\Delta\mathrm{H_s} = \mathrm{H_s}(22\ \mathrm{Feb}) - \mathrm{H_s}(7\ \mathrm{Feb})$. We mask changes over $150\,\mathrm{cm}$ in magnitude (likely caused by lidar voids or canopy returns, 0.03 % of lidar pixels), and then average the $0.5\,\mathrm{m}$ resolution lidar onto the 20 and $80\,\mathrm{m}$ product grids. Every comparison uses the pixels where ΔSWE and $\Delta\mathrm{H_s}$ are both valid. When we need to compare the two in the same units, we convert $\Delta\mathrm{H_s}$ to a lidar-implied SWE using the

https://doi.org/10.5194/egusphere-2026-5140
Preprint. Discussion started: 23 September 2026

SNOTEL new snow density (Sect. 2). This is one density for the whole scene, so the implied SWE carries none of the spatial variation in new snow density the scene may have had, due to limited new snow density observations.

We compare the NISAR ΔSWE and lidar ΔH_s scene-wide and locally. Scene-wide, we take the Pearson correlation over all valid pixels and the centered root-mean-square difference (RMSD) between ΔSWE and the lidar-implied SWE. The interferometric phase carries one unknown offset, so the RMSD is computed after removing the median difference between the two fields. It measures the spread about that offset and not an absolute accuracy, and it is an upper limit on the error in the retrieved pattern, since it also carries the lidar uncertainty and the assumption of a constant new snow density across the scene. We repeat these scene-wide statistics over a sweep of coherence thresholds from 0.2 to 0.5, reporting the fraction of pixels each retained and the implied new snow density. That density is the slope of ΔSWE on ΔH_s: if two areas differ by a meter of depth change and 150 mm of retrieved water, the implied new snow density is $150\,\mathrm{kg\,m^{-3}}$. To separate spatial scales, we decompose each field with a Gaussian filter ($\sigma = 500\,\mathrm{m}$) into a kilometer-scale low-pass component and a sub-kilometer high-pass residual, and calculate the correlation for each pair of filtered scenes.

Locally, we map a 440 m windowed Pearson correlation between ΔSWE and ΔH_s at every pixel. Within each window, pixels contribute with a Gaussian weight whose standard deviation is 110 m, one quarter of the window. The local mean is removed within each window before correlating. We then rank-correlate (Spearman) the window's spatial correlation against the window's coherence, the local incidence angle, and forest canopy fraction (fcf) from ESA WorldCover (Zanaga et al., 2022), and split the windows into burned and unburned ground using the Monitoring Trends in Burn Severity (MTBS) data (Eidenshink et al., 2007). We take 50° as the steep threshold for local incidence angle, which isolates roughly the steepest fifth of the scene.

To assess the unwrapping, we count the pixels that the SNAPHU unwrapping algorithm (Chen and Zebker, 2000) shifted, and the pixels where ΔH_s, converted to phase, would exceed one fringe (2π). Unwrapping adds a whole number of fringes to each pixel's wrapped phase, and the product delivers the unwrapped result but not the number of fringes added during unwrapping. We recover it by complex averaging the 20 m wrapped interferogram to the 80 m unwrapped posting, then subtracting the wrapped phase from the unwrapped phase and rounding to the nearest fringe.

To test whether the 20 m phase holds detail finer than the delivered posting captures, we unwrap that 20 m layer ourselves with SNAPHU, using the delivered coherence and the 18.6 effective looks the ISCE3 estimator returns for the delivered 5 by 6 look interferogram, and convert it with Eq. (1) as above. From it we take three 2.0 by 1.4 km insets (Fig. 3), chosen by hand using the burn-severity and canopy-fraction maps: one inside the burn scar, one across its edge, and one in unburned dense forest. All three sit near the scene median incidence angle, so they contrast canopy and burn rather than viewing geometry. We plot each panel as a departure from its own window median divided by that window's standard deviation, so one color scale serves all six and the insets are compared by spatial pattern rather than by accumulation level. The lidar is upscaled from 0.5 m to a 3 m grid and NISAR is shown at 20 m.

https://doi.org/10.5194/egusphere-2026-5140
Preprint. Discussion started: 23 September 2026

4 Results

Scene-wide, the ΔSWE pattern tracks the airborne lidar ΔH_s (Fig. 2), with $r = 0.82$ over all 4976 common pixels and an RMSD against the lidar-implied SWE of 19 mm. The agreement improves as lower-coherence pixels are excluded. Above a coherence of 0.2, which retains 58 % of the pixels, $r = 0.93$ and the difference falls to 12 mm. Above a coherence of 0.4, retaining 20 % of pixels, $r = 0.96$ and it falls to 9 mm. Figure 2's linear fit slope over all pixels corresponds to an implied new snow density of 141 $\mathrm{kg\,m^{-3}}$, close to the 147 $\mathrm{kg\,m^{-3}}$ SNOTEL new snow density, and the implied density stays between 154 and 160 $\mathrm{kg\,m^{-3}}$ across the coherence thresholds of 0.2 and 0.4. This slope-derived density is an independent check that the retrieved ΔSWE values are reasonable, and is insensitive to the choice of reference phase. Splitting both fields into components above and below $\sim$1 km wavelength (500 m Gaussian low pass and its residual), the over-kilometer components agree closely ($r \approx 0.94$), while the sub-kilometer components have a much lower correlation ($r \approx 0.42$).

The local correlation varies across the scene and is lower for the sub-kilometer windows than for the full scene. It is highest in open and burned ground (median local $r \approx 0.57$ for fcf < 0.5 or burned) and much weaker in dense forest canopy (median ≈ 0.26 for fcf > 0.5 and unburned, about 20 % of windows have $r < 0$) and at steep incidence angles (median ≈ 0.20 above 50° against ≈ 0.46 below, about 25 % of windows have $r < 0$). The local correlation decreases with increasing local incidence angle (Spearman -0.43) and with increasing canopy fraction (-0.32), and increases with increasing coherence ($+0.38$). These factors covary across the scene, so we report the associations but cannot disentangle them.

There was minimal phase wrapping in this scene. Converting ΔH_s to phase, using Eq. (1) and the SNOTEL inferred new snow density, 96 % of pixels fall within one fringe, with a median phase change of 0.45 fringes (0.9π). Consistent with this, unwrapping made few corrections: SNAPHU added one fringe (2π) to 10 % of pixels and two fringes to none.

Scene-wide, the 20 m field we unwrapped correlates with the lidar at $r = 0.75$ over 77178 pixels, against $r = 0.82$ at the delivered 80 m posting. Averaging it back to 80 m gives $r = 0.85$ (Hoppinen et al., 2026). The insets show what these numbers look like on the ground (Fig. 3). Inside the burn scar (1a and 1b, 80 % burned with a canopy fraction of 0.35), ΔSWE reproduces the lidar accumulation pattern hillslope by hillslope ($r = 0.68$ over 6350 pixels, median coherence 0.50). Across the fire edge (2a and 2b, 34 % burned with a canopy fraction of 0.49) the agreement is similar ($r = 0.70$ over 7070 pixels, coherence 0.38). In unburned dense forest (3a and 3b, canopy fraction 0.77) it is weaker ($r = 0.45$ over 6811 pixels, coherence 0.27). All three sit between 32 and 40° of local incidence angle (scene median 38°), so viewing geometry is very similar. Burn extent, canopy fraction and coherence still change together, so the insets show the contrast without isolating its cause. The slope inside each window implies a new snow density of 173 (1), 156 (2) and 147 $\mathrm{kg\,m^{-3}}$ (3). These densities show that the dynamic range, as well as the pattern, is reasonable for new snow accumulation, with the higher density in inset 1 likely due to wind densification in this more exposed terrain.

5 Discussion

For this pair, NISAR L-band ΔSWE reproduces the airborne lidar ΔH_s pattern across the scene. The scene-wide agreement is strong, but is primarily carried by the over-kilometer component, largely driven by elevation at this site ($r \approx 0.94$) and less so by

https://doi.org/10.5194/egusphere-2026-5140
Preprint. Discussion started: 23 September 2026

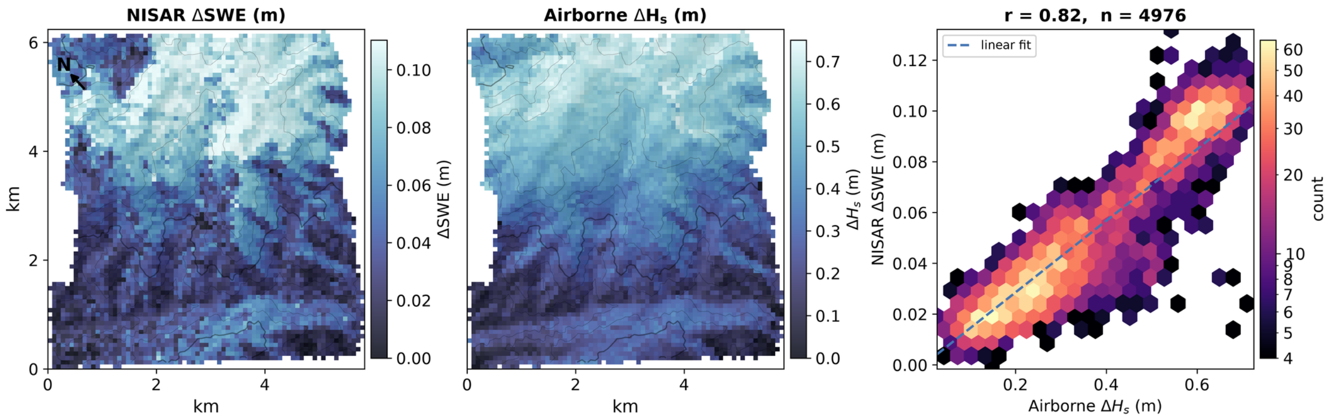

Figure 2. Full-scene comparison from the operational NISAR interferogram, every panel at the delivered 80 m unwrapped posting. Maps of NISAR $\Delta\mathrm{SWE}$ and NIVAL lidar $\Delta\mathrm{H_s}$, and the density scatter of $\Delta\mathrm{H_s}$ versus $\Delta\mathrm{SWE}$ over all common pixels, with the Pearson correlation.

the sub-kilometer component ($r \approx 0.42$), likely controlled by wind and vegetation. The RMSD against the lidar-implied SWE is 19 mm, though it is computed after centering and assumes one new snow density across the scene, so it leans on assumptions the spatial correlations do not. Excluding the least coherent pixels improves the agreement, and both the correlation and the difference from the lidar level off near a coherence of 0.4, at a correlation of 0.96 and a difference below 1 cm SWE. The retrieved density is stable across those thresholds, so the gating selects pixels with less phase noise rather than a different population of snow.

Several conditions made this a favorable pair. The accumulation produced a measurable phase change yet stayed within one fringe, so little unwrapping was needed. The snowpack was cold and dry during both acquisitions, so the dry-snow assumption holds, and there was no melt or rain between them that could have lowered coherence. The atmosphere was quiet: the RAiDER tropospheric delay has an elevation trend of only about 1 % of the snow elevation phase ramp, and the inter-pass ionospheric change was small (0.8 total electron content units, TECU, in the lowest fifth of 12-day changes at this mid-latitude site). Winds stayed below the drift threshold off the ridgelines, so accumulation likely varied smoothly relative to the InSAR pixels, helping to keep coherence high (Hoppinen et al., 2026). These conditions are not guaranteed in other pairs or seasons. Of the seven candidates on this track between November and March, this was the only pair that was dry at both acquisitions, so it is the one we could analyze. The comparison therefore shows what the retrieval can do under favorable conditions and not how often those conditions arise.

Within the scene, the local correlation is highest in open and burned ground and lowest under dense forest (Fig. 3), and it falls as the local incidence angle steepens (Sect. 4). This matches previous work on InSAR SWE retrievals (Bonnell et al., 2024). Vegetation degrades the retrieval through temporal and volumetric decorrelation and a canopy phase bias (Zwieback and Hajnsek, 2016; Palomaki et al., 2026). Steep incidence angles cause thermal decorrelation as the backscatter and signal-

https://doi.org/10.5194/egusphere-2026-5140
Preprint. Discussion started: 23 September 2026

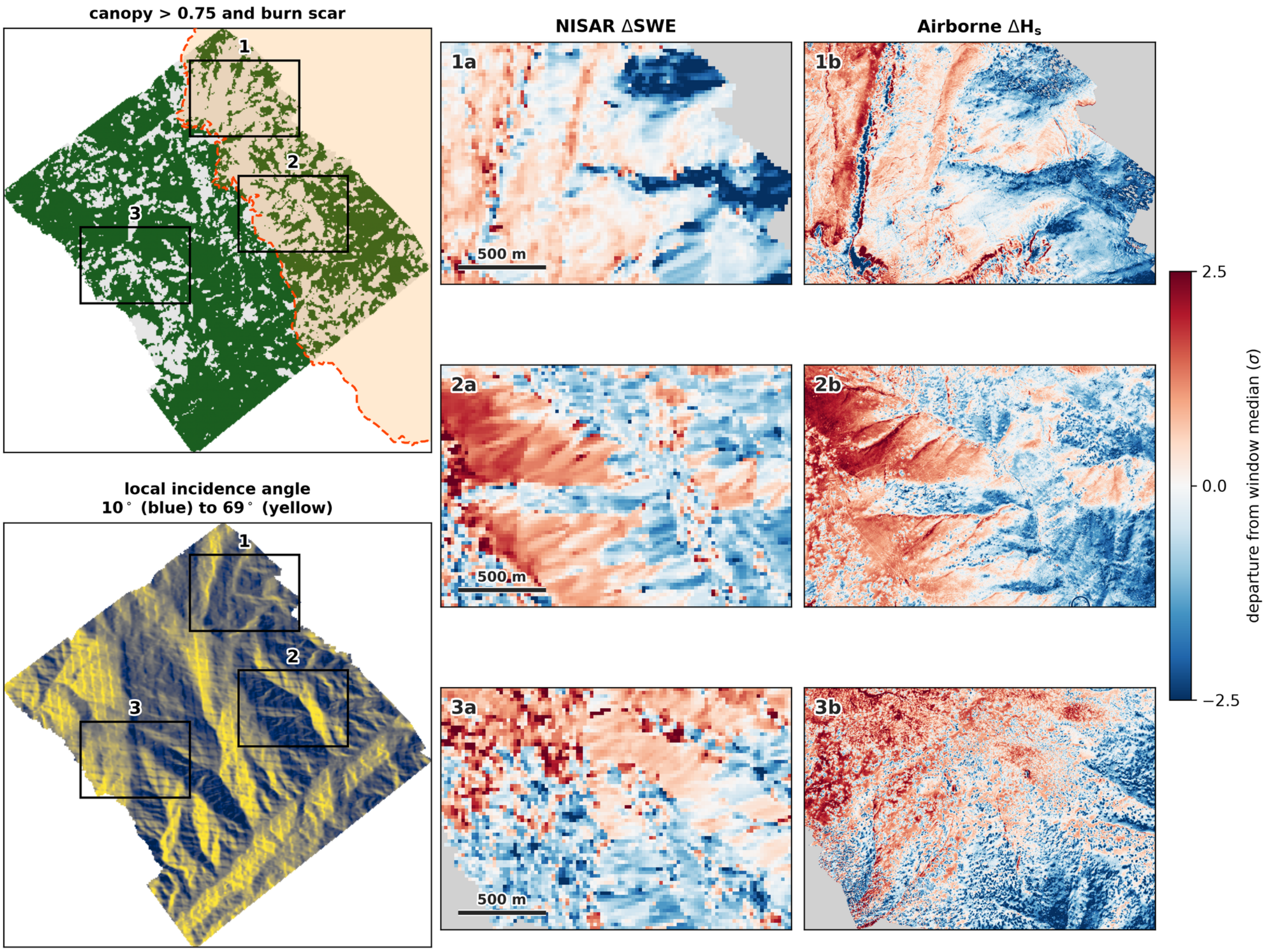

Figure 3. NISAR ΔSWE and lidar ΔH_s over three 2.0 by 1.4 km insets, from the 20 m wrapped interferogram unwrapped with SNAPHU. Left, canopy fraction above 0.75 and the local incidence angle, with the 2016 Pioneer Fire perimeter dashed and its burned side shaded. Right, NISAR (a) and lidar (b) for each inset, as departures from the panel's own median in standard deviations, so one color scale serves all six. The lidar is shown at 3 m resolution and NISAR at 20 m. Inset 1 is in open terrain inside the burn scar, 2 near its edge, and 3 in unburned dense forest.

to-noise ratio decrease. Wind is not a primary cause of the weaker local correlation except potentially at the highest elevations, since the area below ridgelines stayed below the drift threshold (Sect. 2).

This study has limitations. First, the lidar pair spans 15 days compared to the 12-day radar pair. The three extra days add only about 5 mm of SWE at the co-located SNOTEL, compared to the 56 mm accumulated over the radar pair, a mismatch of about 9 %. Second, we compared ΔSWE against ΔH_s by correlation and did not estimate a spatially varying new snow density field, which a full conversion would require. Coincident, spatially distributed field observations of density should be

https://doi.org/10.5194/egusphere-2026-5140
Preprint. Discussion started: 23 September 2026

prioritized in future NISAR validation efforts. Settlement complicates that conversion: the standing pack loses depth but not SWE, and deeper packs settle more, so ΔH_s and ΔSWE are not linearly related during the settlement period, which can be significant for 48 hours following large storms. Third, we do not account for lidar uncertainties. Finally, this is one pair at one site. The full mission's systematic acquisitions will extend validation to more pairs, sites, and snow conditions.

6 Conclusions

Evaluated against airborne lidar, NISAR L-band interferometry recovers the pattern of snow accumulation across this mountain scene. Agreement is strong at kilometer scales ($r \approx 0.94$) and degrades toward sub-kilometer scales ($r \approx 0.42$), where forest canopy and steep incidence angles limit the retrieval. Defining where the retrieval continues to work will require more pairs across more terrain and snow conditions. These results provide the first direct evidence that NISAR phase can measure dry-snow accumulation.

Code and data availability. The analysis code, the pair census and the supplement figures are available at https://github.com/ZachHoppinen/nival_validation. The NIVAL airborne-lidar snow-depth product is distributed by the National Snow and Ice Data Center (NSIDC) (https://doi.org/10.5067/DPFDH2M49DQG). The NISAR L2 interferometric product used here is distributed by the Alaska Satellite Facility (https://doi.org/10.5067/NIL2GUNW-P1), granule NISAR_L2_PR_GUNW_012_077_A_024_013_4000_SH_20260207T124619_20260207T124654_20260219T124619_20260219T124654_P05023_N_F_J_001. SNOTEL records are available from the USDA Natural Resources Conservation Service (NRCS). Data from the Freeman station, including the snowpack temperature profile and the meteorological record, are available from the authors on request. The ancillary public datasets used (ESA WorldCover, MTBS burn severity, USDA NAIP imagery, the Copernicus GLO-30 DEM, and International GNSS Service (IGS) Global Ionosphere Maps) are available from their respective providers and cited in the text.

Author contributions. ZH: conceptualization, methodology, formal analysis, visualization, writing (original draft). HPM, CK, TVDW, and SC: data curation, resources, writing (review and editing). RP and SO: writing (review and editing).

Competing interests. The authors declare that they have no conflict of interest.

Acknowledgements. This work used provisional data made available by the NASA-ISRO SAR (NISAR) mission, obtained from the Alaska Satellite Facility DAAC.

The coincident lidar surveys were collected for the NIVAL project, which supported 12 surveys and processing during WY 2026, near coincident with NISAR, under NASA grant 80NSSC25K0132 (HPM, SO, TVDW, SC). We leveraged field observations supported by CRREL grant W913E524C0015 (HPM). We thank the NIVAL field and flight team for collecting the field and lidar surveys.

https://doi.org/10.5194/egusphere-2026-5140
Preprint. Discussion started: 23 September 2026

The authors used Anthropic's Claude to assist with figure-generation code and manuscript text editing.

Financial support. This work was supported by NASA grants 80NSSC25K7452 (ZH, RP, HPM) and 80NSSC25M7047 (HPM).

https://doi.org/10.5194/egusphere-2026-5140
Preprint. Discussion started: 23 September 2026

References

Belinska, K., Fischer, G., Nagler, T., and Hajnsek, I.: Snow Water Equivalent Estimation Using Differential SAR Interferometry and Co-Polar Phase Differences from Airborne SAR Data, in: IGARSS 2022 - 2022 IEEE International Geoscience and Remote Sensing Symposium, pp. 4545–4548, https://doi.org/10.1109/igarss46834.2022.9883110, 2022.

Bonnell, R., Elder, K., McGrath, D., Marshall, H. P., Starr, B., Adebisi, N., Palomaki, R. T., and Hoppinen, Z.: L-Band InSAR Snow Water Equivalent Retrieval Uncertainty Increases With Forest Cover Fraction, Geophysical Research Letters, 51, https://doi.org/10.1029/2024gl111708, 2024.

Chen, C. W. and Zebker, H. A.: Network approaches to two-dimensional phase unwrapping: intractability and two new algorithms, Journal of the Optical Society of America A, 17, 401–414, https://doi.org/10.1364/josaa.17.000401, 2000.

Dozier, J., Bair, E. H., and Davis, R. E.: Estimating the spatial distribution of snow water equivalent in the world's mountains, WIREs Water, 3, 461–474, https://doi.org/10.1002/wat2.1140, 2016.

Eidenshink, J., Schwind, B., Brewer, K., Zhu, Z.-L., Quayle, B., and Howard, S.: A Project for Monitoring Trends in Burn Severity, Fire Ecology, 3, 3–21, https://doi.org/10.4996/fireecology.0301003, 2007.

European Space Agency and Airbus: Copernicus DEM, https://doi.org/10.5270/esa-c5d3d65, 2021.

Fattahi, H., Gunter, G., Hawkins, B., Burns, R., Brancato, V., Shiroma, G. H., Ghaemi, H., Huang, B., Jung, J., Huang, X., Niemoeller, S. C., Hudson, T., Staniewicz, S. J., Jeong, S., Aivazis, M., Rosen, P., and Lavalle, M.: ISCE3: InSAR Scientific Computing Environment Enhanced Edition, AGU Fall Meeting 2023, abstract G23C-0488, 2023.

Guneriussen, T., Høgda, K. A., Johnsen, H., and Lauknes, I.: InSAR for Estimation of Changes in Snow Water Equivalent of Dry Snow, IEEE Transactions on Geoscience and Remote Sensing, 39, 2101–2108, https://doi.org/10.1109/36.957273, 2001.

Hernandez-Pajares, M., Juan, J. M., Sanz, J., Orus, R., Garcia-Rigo, A., Feltens, J., Komjathy, A., Schaer, S. C., and Krankowski, A.: The IGS VTEC maps: a reliable source of ionospheric information since 1998, Journal of Geodesy, 83, 263–275, https://doi.org/10.1007/s00190-008-0266-1, 2009.

Hoppinen, Z., Zwieback, S., Palomaki, R., and Marshall, H.-P.: Snow accumulation variability limits InSAR SWE retrieval, EGUsphere [preprint], https://doi.org/10.5194/egusphere-2026-3772, 2026.

Leinss, S., Wiesmann, A., Lemmetyinen, J., and Hajnsek, I.: Snow Water Equivalent of Dry Snow Measured by Differential Interferometry, IEEE Journal of Selected Topics in Applied Earth Observations and Remote Sensing, 8, 3773–3790, https://doi.org/10.1109/jstars.2015.2432031, 2015.

Li, L. and Pomeroy, J. W.: Estimates of Threshold Wind Speeds for Snow Transport Using Meteorological Data, Journal of Applied Meteorology, 36, 205–215, https://doi.org/10.1175/1520-0450(1997)036<0205:EOTWSF>2.0.CO;2, 1997.

Maurer, J., Bekaert, D., Sangha, S., Hamlington, B., Marshak, C., Lei, Y., Kumar, P., and Fattahi, H.: RAiDER: Raytracing Atmospheric Delay Estimation for RADAR, AGU Fall Meeting 2021, abstract G44A-07, 2021.

Nagler, T., Rott, H., Scheiblauer, S., Libert, L., Mölg, N., Horn, R., Fischer, J., Keller, M., Moreira, A., and Kubanek, J.: Airborne Experiment on InSAR Snow Mass Retrieval in Alpine Environment, in: IGARSS 2022 - 2022 IEEE International Geoscience and Remote Sensing Symposium, pp. 4549–4552, https://doi.org/10.1109/igarss46834.2022.9883809, 2022.

Palomaki, R., Hoppinen, Z., and Marshall, H.-P.: A spatiotemporal analysis of errors in InSAR SWE measurements caused by non-snow phase changes, The Cryosphere, 20, 2703–2721, https://doi.org/10.5194/tc-20-2703-2026, 2026.

https://doi.org/10.5194/egusphere-2026-5140
Preprint. Discussion started: 23 September 2026

Rosen, P. A., Hensley, S., Shaffer, S., Veilleux, L., Sagi, V. R., Satish, R., Chakraborty, M., Misra, T., and Bhan, R.: The NASA-ISRO SAR Mission: An International Space Partnership for Science and Societal Benefit, in: 2015 IEEE Radar Conference (RadarCon), pp. 1610–1613, https://doi.org/10.1109/radar.2015.7131255, 2015.

Ruiz, J. J., Merkouriadi, I., Lemmetyinen, J., Cohen, J., Kontu, A., Nagler, T., Pulliainen, J., and Praks, J.: Comparing InSAR Snow Water Equivalent Retrieval Using ALOS2 With In Situ Observations and SnowModel Over the Boreal Forest Area, IEEE Transactions on Geoscience and Remote Sensing, 62, 1–14, https://doi.org/10.1109/tgrs.2024.3439855, 2024.

Van Der Weide, T., Ciafone, S., Wadhwani, Y., Alabi, I., O'Neel, S., and Marshall, H.-P.: NIVAL Mores Creek Summit Snow Depth, Canopy Height, and DTM from Airborne LiDAR, NASA National Snow and Ice Data Center Distributed Active Archive Center [data set], Boulder, Colorado, USA, https://doi.org/10.5067/DPFDH2M49DQG, 2026.

Zanaga, D., Van De Kerchove, R., Daems, D., De Keersmaecker, W., Brockmann, C., Kirches, G., Wevers, J., Cartus, O., Santoro, M., Fritz, S., Lesiv, M., Herold, M., Tsendbazar, N.-E., Xu, P., Ramoino, F., and Arino, O.: ESA WorldCover 10 m 2021 v200, https://doi.org/10.5281/zenodo.7254221, 2022.

Zwieback, S. and Hajnsek, I.: Influence of Vegetation Growth on the Polarimetric Zero-Baseline DInSAR Phase Diversity—Implications for Deformation Studies, IEEE Transactions on Geoscience and Remote Sensing, 54, 3070–3082, https://doi.org/10.1109/tgrs.2015.2511118, 2016.